Advanced Steel Construction – Vol. 21 No. 5 (2025) 380–389
DOI:10.18057/IJASC.2025.21.5.2

OPTIMAL DESIGN AND CONSTRUCTION OF A STEEL ARCHED PEDESTRIAN BRIDGE WITH STRUCTURAL ENHANCEMENT USING UHPC ENCASEMENT

Canh-Tuan Nguyen *

Faculty of Civil Engineering, Ho Chi Minh City University of Technology (HCMUT)-Vietnam National University Ho Chi Minh City (VNU-HCM)
** (Corresponding author: E-mail: ctnguyen@hcmut.edu.vn)*

ABSTRACT

This study focused on improving the structural design and reducing the costs of steel arched pedestrian bridges through detailed analysis and practical application. Optimization techniques were applied to identify the best sectional sizes and configurations for steel arch bridges, revealing that the arch ribs were sensitive to lateral buckling due to their high slenderness. To counter this and enhance the load-carrying capacity and stability, the arch ribs were proposed to be encased with Ultra-High-Performance Concrete (UHPC), especially near the bearings where the free length is substantial. Through non-linear finite element analysis, this study assessed the method's impact on buckling behavior, strength enhancement, and stress distribution within the arch ribs. The application of this solution in an actual construction project highlights its practicality and efficiency for pedestrian bridge development. Furthermore, the research contributes significantly to creating specialized manufacturing and construction methods for steel arched bridges, presenting an encouraging strategy for future applications.

ARTICLE HISTORY

Received: 25 April 2024
Revised: 4 February 2025
Accepted: 6 February 2025

KEYWORDS

Load-carrying capacity;
Stability enhancement;
Steel arched bridge;
Optimal design;
UHPC integration

1. Introduction

Steel arch constructions are highly preferred for pedestrian bridges, not only for their visual appeal but also for their structural effectiveness. The arch elements are crucial in bearing external forces, highlighting the importance of finding optimal designs that feature compact sections. This approach enhances the resistance to buckling and optimizes the structure's capacity to support loads. Addressing the risk of buckling in steel arch bridges is vital for maintaining structural integrity, safety, and overall functionality. Buckling, a frequent issue in such structures, occurs when slender arch components are subjected to compressive stress along their length. Maintaining stability to avert sudden and catastrophic failures is imperative. Extensive research has been dedicated to exploring the buckling behavior of steel arches, including studies on both in-plane and out-of-plane inelastic buckling. These efforts aim to refine predictive models for accurately determining the buckling strength of steel arches [1-5].

Buckling directly influences the load-carrying capacity of a steel arched bridge. Understanding the critical buckling modes and loads allows engineers to determine the maximum loads that the bridge can safely withstand without experiencing structural instability. This information is important for the design and assessment of the bridge's capacity to support various loads. Explorations into the impact of buckling on the load-carrying capacity of steel arches have been conducted. Pi et al. [6] explored the nonlinear in-plane buckling and post-buckling behavior to investigate influences of pre-buckling deformations on the overall behavior of steel arches. Multiple inquiries have examined the impact of bracings on the buckling strength of steel arches. Pi et al. [7] and Dou et al. [8, 9] focused on the influence of bracing stiffness from both lateral and rotational braces, on the elastic out-of-plane flexural-torsional buckling of steel circular arches. The research has revealed that enhancing bracing stiffness could effectively improve the strength of steel arches emphasizing that the slenderness of the arches is the pivotal factor in preventing buckling.

Optimization studies have been conducted to improve the structural performance of steel arched bridges, including the analysis of different arch geometries, support systems, and load distribution mechanisms. Finite element analysis (FEA) and computational tools effectively aid in assessing and refining these structures such as advanced analysis of inelastic buckling and post-buckling behavior. By understanding the buckling behavior, engineers can explore design modifications, such as adjusting the arch geometry, combining materials, or incorporating additional structural elements, to enhance the overall performance of the steel arched bridges. Nazmy [10] introduced an optimal methodology that comprehensively accounts for the impacts of diverse design parameters on both the strength and stability of steel arch bridges. Additionally, the optimal design of steel arch bridges has been addressed through the application of genetic algorithms, aiming to minimize the dimensions of the primary steel members [11, 12]. Numerous other investigations on optimization have been performed for various types of arched bridge, including arched trusses and funicular twin arches [13-15].

Extensive research has been dedicated to enhancing the materials used in steel arched bridges, with a focus on incorporating advanced materials such as high-strength steels, high-performance concrete, and fiber-reinforced composites. The aim is to improve the performance of steel arch bridges by achieving higher strength-to-weight ratios and enhancing their resistance and durability. This effort seeks to prolong the operational lifespan of bridges, addressing the critical need for sustained structural functionality. Researchers are exploring the optimal application of composite materials to boost the structural efficiency and carrying capacity of these bridges. This includes investigating various configurations, cross-sectional shapes, and combinations of materials to attain optimal performance under different loading scenarios. The study of composite arch members, which combine steel with materials like concrete or fiber-reinforced polymers, is particularly active. This research examines the structural behavior, load distribution, and longevity of composite arch elements versus traditional steel-only versions. Concrete-filled steel tubular arches, which blend steel's strength and durability with concrete's load-bearing capacity, represent a significant innovation in structural engineering. These arches feature a steel tube filled with concrete to create a composite structure that leverages the benefits of both materials. Additionally, this approach allows for efficient material use, leading to more sustainable and cost-effective construction practices [16-21]. The synergy of material properties in these arches enables them to cover large spans with few supports, offering an efficient and aesthetically pleasing solution for infrastructure projects. Discussions have also covered the advantages and limitations of Ultra-High-Performance Concrete (UHPC) in bridge construction. UHPC's exceptional mechanical properties and durability enhance the structural integrity of bridge connections, mitigate deformation and cracking in bridge pavements, and increase the load-bearing capacity of bridges [22].

The use of UHPC in structural design has been increasingly supported by life-cycle cost analysis (LCCA) to highlight its economic and sustainability benefits. A key study by Hossain and Chang [23] demonstrated that UHPC significantly reduces maintenance frequency and overall life-cycle costs in bridge retrofitting compared to conventional concrete alternatives. Their analysis showed that despite higher initial costs, UHPC's extended service life, up to 80 years compared to 30 years for conventional concrete, substantially decreases long-term expenditures. Similarly, Dong [24] evaluated UHPC's performance in terms of cost-effectiveness, environmental impacts, and durability. The study emphasized UHPC's ability to reduce CO2 emissions and maintenance requirements over the lifecycle of structures, making it a sustainable alternative for infrastructure projects. The application of UHPC in precast girders demonstrated reductions in material volume and associated environmental impact. Furthermore, Stengel and Schießl [25] conducted an extensive LCCA to compare UHPC with traditional materials in various structural applications, including bridges. Their findings indicated that UHPC's higher strength and durability enable smaller cross-sections, reducing material consumption and long-term costs despite the energy-intensive production

process. These studies collectively support the economic and environmental viability of UHPC in modern construction, particularly for projects emphasizing durability and cost-efficiency in constrained environments. Such findings align with the methodology and outcomes of this study, reinforcing the relevance of UHPC in sustainable infrastructure development.

This study aims to address this gap by proposing a novel design and construction scheme that integrates Ultra-High-Performance Concrete (UHPC) with steel arches, optimizing both performance and cost for a specific project in a remote mountainous region. Unlike previous research, which primarily focuses on large-scale infrastructure or generalized design improvements, this study is tailored to the unique constraints of constructing pedestrian bridges in challenging environments. By leveraging finite element analysis and practical construction methods, we developed an optimized configuration for steel-UHPC composite arch structures. This approach not only enhances load-carrying capacity and stability but also minimizes costs, making it an accessible solution for underprivileged communities. Additionally, the research demonstrates the feasibility of implementing such designs under strict financial and temporal constraints, contributing to a broader understanding of how advanced materials like UHPC can be utilized in cost-sensitive applications. The project is distinguished by its focus on practical application, culminating in the successful construction of a pedestrian bridge that serves as a vital connection for a remote community. This achievement underscores the potential for replicating and scaling the proposed methodology in similar contexts, addressing a critical need for sustainable and affordable infrastructure.

2. Optimum design of the steel arched structure

2.1. Structural optimization approach

The collapse of an existing suspension bridge posed a significant divide between communities on either side of the spring, necessitating a new bridge for the local people. A steel tied arch bridge, chosen for its aesthetic appeal that enhances the local tourism landscape, was proposed. This new bridge, designed to be 39 meters long and 2.3 meters wide for walkway, could support a standard pedestrian load of 4.3 kN/m in accordance with the LRFD Guide Specifications for the Design of Pedestrian Bridges [26]. Owing to various constraints at the site of construction, the height of the steel arch should be restricted to 5.0 meters, resulting in a height-to-span ratio for the steel arch of only 0.128. The objective of this study was to identify a design solution that not only meets the criteria for cost efficiency but also ensures practicality in construction processes and strict compliance with project schedule within four months. To accommodate the transportation and erection requirements under local conditions, it was determined that the steel arch structure needs to be segmented into pieces no longer than 6.0 meters each. A thorough cost analysis, considering the fabrication expenses of the steel structures, the costs associated with structural connections, and the erection method, was conducted. The general alignment of the bridge is illustrated in Fig. 1.

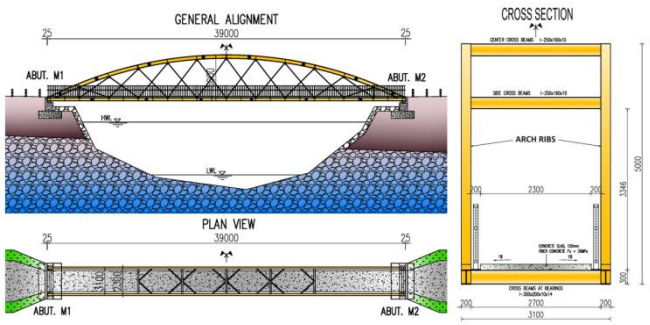

Fig. 1 General alignment of the steel arch bridge

The optimization of arch structures can be approached through various methods, each with its unique focus and application. These methods often aim at enhancing structural efficiency, reducing material usage, or improving the overall performance of the structure under different loading conditions. In the design of the steel arch structure, which comprises arch ribs, tie girders, floor beams, and hangers, structural analyses and partial optimization process was undertaken. This process was grounded in the principle of balancing construction costs while ensuring structural integrity and efficiency. The general process of the structural optimization process is described in Fig. 2.

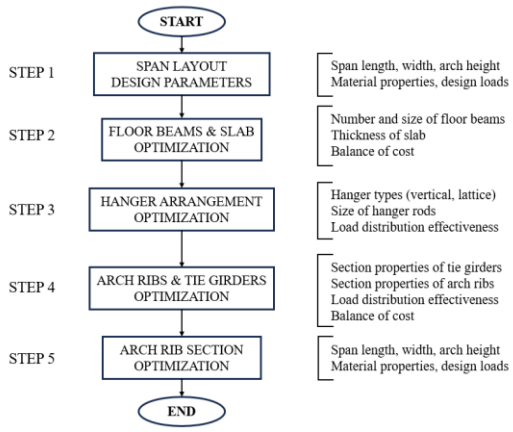

Fig. 2 Optimization process of the steel arch bridge

The optimization process was efficiently conducted with the aid of the finite element analysis program MIDAS CIVIL. To accurately simulate the structural components, beam elements were employed for arch ribs, tie girders and floor beams; tension-only truss elements for hangers; and truss elements for bracing components. Subsequently, internal forces were carefully obtained to facilitate the design of each section. The configuration of the simulation model is presented in Fig. 3.

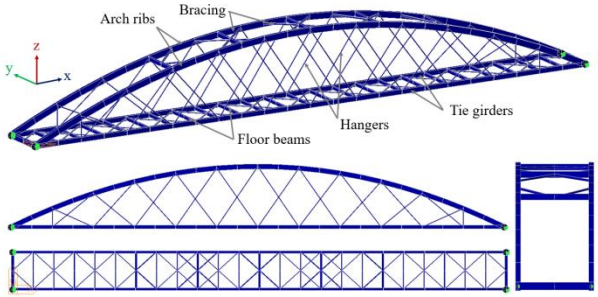

Fig. 3 Finite element model for optimization analysis

2.2. Results of optimal design

2.2.1. Floor beams and concrete slab

The parametric optimization method was conducted to find the best combination of the number and dimensions of floor beams, the thickness of the concrete slab, and the amount of reinforcing bar (rebar) within the slab. The number of floor beams was also found to have a significant impact on the alignment of the hanger system. The optimal design should be achieved not only to meet structural integrity and safety standards but also to minimize construction and material costs.

A target function for the optimal cost is defined from the total construction costs of floor beams and the concrete slab as follows:

$$C = \min\left(C_b + C_s\right) \tag{1}$$

Where $C_b = f(q_{PL}, N_b, L_b, A_b, S_{x,b}, f_y, c_b)$ is the cost of floor beams, and is a function of the pedestrian load q_{PL}, number of floor beams N_b, length of floor beams L_b, sectional area of floor beams A_b, section modulus $S_{x.b}$, yield strength f_y = 250 MPa, and unit cost for fabrication and construction of steel beams c_b; $C_s = f\left(q_{PL}, S_b, b_s, t_s, A_r, f_y, f_c', c_c, c_r\right)$ is the cost of the reinforced concrete slab, and is a function of the pedestrian load, floor beam spacing S_b, slab width b_s, slab thickness t_s, rebar area A_r, yield strength of rebar f_y = 400 MPa, compressive strength of concrete f_c' = 28 MPa, unit cost for concrete c_c and for rebar c_r.

To obtain the optimal design, strength constraints for floor beams and the slab should be defined. For the reinforced concrete slab, the factored bending moment in the slab $M_{Str,s}$ at the Strength Limit State should satisfy:

$$M_{Str,s} \le \phi A_r f_y \left(t_s - 0.59 \frac{A_r f_y}{f_c' b_s} \right) \quad (2)$$

For floor beams, the factored bending moment in floor beams $M_{Str,b}$ at the Strength Limit State should satisfy:

$$M_{Str,b} \le f_y S_{x,b} \quad (3)$$

Additional contraints for cross-section proportion limits including web and flange of floor beams should be considered in accordance with Clause 6.10.2 from AASHTO LRFD design code [27] for I-section flexural members.

In the process of parametric optimization, the characteristics of floor beams and slabs were directly influenced by a specific set of parameters which were optimized using an iteration method to satisfy the constraints from Eqs. (2) and (3) with minimum cost. This optimization could identify the minimum cost from these sets by using Eq. (1). The sequence of steps taken in this optimization process is clearly outlined in Fig. 4, and the results of the optimal design parameters for varying numbers of floor beams are detailed in Table 1.

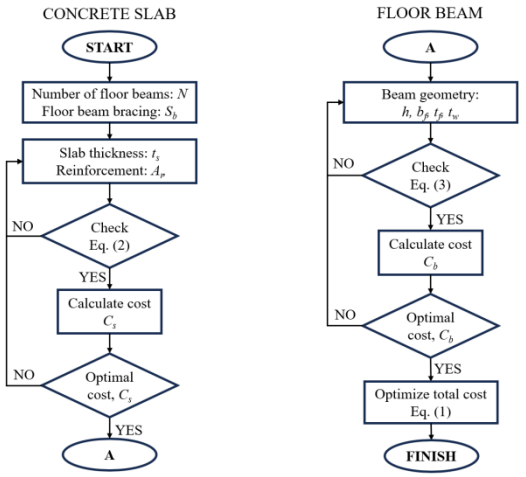

Fig. 4 Parametric optimization process for floor beams and slab

Table 1
Design data for cost optimization of floor beams and reinforced concrete slab

Variables	Optimal parameters for floor beams and slab								
N_b	40	33	29	25	23	21	19	17	16
S_b (m)	1	1.2	1.4	1.6	1.8	2	2.2	2.4	2.6
t_s (m)	0.08	0.08	0.1	0.12	0.12	0.15	0.15	0.18	0.18
A_r (mm^2)	159	230	236	253	321	320	388	396	464
h (mm)	100	100	100	125	125	150	150	150	175
b_f (mm)	51	63	80	71	82	77	86	103	91
t_f (mm)	8	8	8	8	8	8	8	8	8
t_w (mm)	5	5	5	5	5	5	5	5	5

It was observed that increasing the number of floor beams led to a reduction in the span length of the slab. This adjustment had a dual effect on the cost structure: while the cost associated with the floor beams increased due to the higher quantity required, there was a consequential decrease in the cost of the concrete slab. The reduction in slab cost can be attributed to the decreased span, which in turn reduces the slab thickness and the amount of rebar needed to meet structural demands. Through a detailed examination depicted in Fig. 5, the minimum total cost could be identified when the ideal number of floor beams is set to 25, with the slab spanning intervals of 1.6 meters and having a thickness of 120 mm.

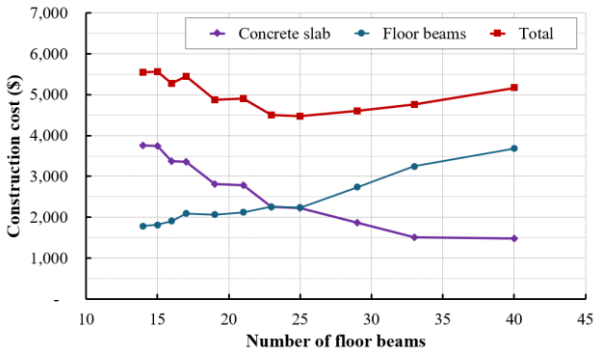

Fig. 5 Variation of optimal cost with different number of floor beams

2.2.2. Hanger members

The optimization of the hanger system in steel arch structures was evaluated by comparing the structural performance of lattice and vertical arrangements in the same loading condition. Two different finite element models were adopted to non-linear analyses to verify the structural performance using ABAQUS [28]. Fig. 6 reveals that the lattice configuration offers effective load distribution capabilities, with buckling confined to the arch ribs near the bearing locations after peak loads are applied. In contrast, the vertical hanger system fails to provide adequate load-carrying capacity, resulting in global buckling across the entire structure. Further comparative analysis, as shown in Fig. 7, demonstrates that the lattice system significantly outperforms the vertical system, with a load capacity of 1760 kN compared to the vertical system's 996 kN, showing a nearly 77% increase in capacity with a similar quantity of materials used. Based on these findings, the lattice system is identified as the optimal solution for steel arch structures, offering superior structural performance and efficiency.

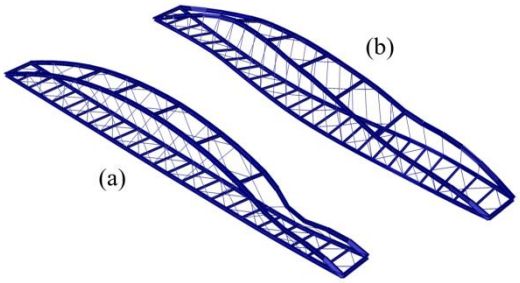

Fig. 6 Buckling of arch ribs with hanger arrangements: (a) lattice type; (b) vertical type

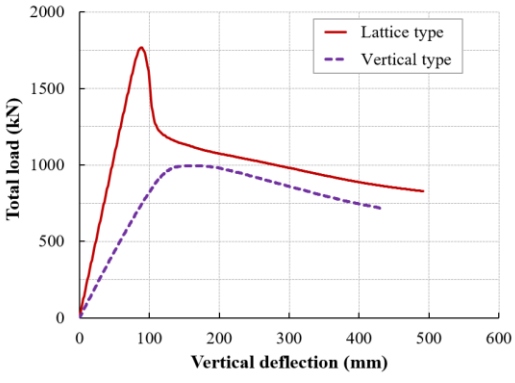

Fig. 7 Load-deflection curves of the steel arch bridge with different types of hangers

2.2.3. Arch ribs and tie girders

After successfully optimizing the floor beams, slab, and hanger system, the overall alignment of the structure was clearly established. It was assumed that cross beams of arch ribs and bracing components were excluded from the optimization process. The next step was to identify the ideal dimensions for arch ribs and tie girders. Critical analyses in the structural optimization of arch bridges revealed a significant correlation between tie girders and arch ribs concerning load distribution, particularly in relation to their rigidities.

Applying Clause 6.8.2.3 and Clause 6.9.2.2 from AASHTO LRFD Design Specification [27] for strength constraints, tie girders subjected to combined

tension and flexure and arch ribs subjected to combined axial compression and flexural shall satisfy:

$$k = \frac{P_u}{2P_r} + \left(\frac{M_{ux}}{M_{rx}} + \frac{M_{uy}}{M_{ry}}\right) \quad \text{if} \quad \frac{P_u}{P_r} < 0.2 \tag{4-1}$$

$$k = \frac{P_u}{P_r} + \frac{8}{9}\left(\frac{M_{ux}}{M_{rx}} + \frac{M_{uy}}{M_{ry}}\right) \quad \text{if} \quad \frac{P_u}{P_r} \geq 0.2 \tag{4-2}$$

Where k is the strength factor that should not exceed 1.0; P_u is the ultimate axial force (kN); P_r is the factored axial resistance (kN) which defined from Clause 6.8.2.1 for tension and Clause 6.9.4.1 for compression respectively [24]; M_{ux} and M_{uy} are the ultimate bending moments about x axis and y axis, respectively (kN.m); M_{rx} and M_{ry} are factored flexural resistances about x axis and y axis, respectively (kN.m). The calculations of Mrx and Mry are detailed in the commentary C6.8.2.3 [27].

Local buckling of arch ribs in compression should be controlled through the limits of the slenderness in accordance with Clause 6.9.4.2 from AASHTO provision [27]. The slenderness of web plates shall satisfy:

$$\lambda_w = D / t_w \leq k_0 \sqrt{E_s / f_y} \tag{5}$$

Where D is web depth (mm); t_w is web thickness (mm); and k_0 is the plate buckling coefficient, k_0 = 1.49.

The slenderness of the half-width flanges of built-up I-sections shall satisfy:

$$\lambda_{fl} = b_f / 2t_f \leq 0.64\sqrt{k_c E_s / f_y} \tag{6}$$

Where b_f is flange width (mm); t_f is flange thickness (mm); and $0.35 \leq k_c \leq 0.76$ in which $k_c = 4/\sqrt{D/t_w}$.

In addition, the structure should satisfy the constraint for the vertical deflection which is specified in Clause 2.5.2.6.2 [24] using load combination at the service limit state. The maximum deflection of the bridge shall not exceed 1/1000 of the span length. Vibrations shall be investigated as a service limit state. Vibration of the structure shall not cause discomfort or concern to users of a pedestrian bridge. The fundamental frequency in a vertical mode of the pedestrian bridge without live load shall be greater than 3.0 Hz to avoid the first harmonic [26].

A vector representing types of I-shaped sections is defined as follows:

$$\mathbf{I}^{\mathrm{T}} = \left[\mathbf{I}_1, \mathbf{I}_2, ..., \mathbf{I}_n\right] \tag{7}$$

Where $\mathbf{I}_i^T = \left[h_i, b_{fl,i}, t_{fl,i}, t_{w,i}\right]$ is a vector of the ith sectional dimensions; h_i is the height (mm); $b_{f,i}$ is the flange width (mm); $t_{f,i}$ is the flange thickness (mm); and $t_{w,i}$ is the web thickness (mm).

Vectors of internal forces, deflections, and natural frequencies corresponding to the ith combination of sections as input parameters for optimization process are defined as follows:

$$\mathbf{F}_i^T = \left[N_i^{rib}, M_i^{rib}, N_i^{tie}, M_i^{tie}, \delta_i, f_i\right] \tag{8}$$

Where N_i^{rib} is the maximum factored axial compression force in arch ribs (kN); M_i^{rib} is the maximum factored bending moment in arch ribs (kN.m); N_i^{tie} is the maximum factored axial compression force in tie girders (kN); M_i^{tie} is the maximum factored bending moment in tie girders (kN.m); δ_i is the maximum vertical deflection (mm); f_i is the natural frequency of the first vertical vibration mode. It is noted that internal forces, deflections, and natural frequencies are outputs of finite element analyses which can be automatically performed by a self-developed coding program including optimization algorithms using Matlab. However, developing such a program would be considered in another study.

Vectors of output results corresponding to the ith combination of sections including slenderness ratios, strength factors, deflections, and natural frequencies for checking violation condition are defined as follows:

$$\mathbf{K}_i^T = \left[\lambda_i^{w,rib}, \lambda_i^{fl,rib}, \lambda_i^{w,tie}, \lambda_i^{fl,tie}, k_i^{rib}, k_i^{tie}, \delta_i, f_i\right] \tag{9}$$

Where λ_i^{rib} and λ_i^{tie} are slenderness ratios of webs and flanges corresponding to the ith combination of sections; kirib and kitie are strength factors of arch ribs and tie girders, respectively.

Fig. 8 describes the process of parametric optimization for tie girders and arch ribs. From given sets of sectional parameters, trial sections were assigned to tie and rib members in the finite element model. Factored axial compression forces and factored bending moments were extracted to calculate strength factors of tie girders and arch ribs. Variations in strength factors of tie girders and arch ribs according to Eq. (4) with different section properties were investigated. The optimization algorithm was developed to find a range of section geometries that could satisfy the strength, slenderness, and deflection constraints with minimum weight of steel material of arch ribs and tie girders.

In the analysis of arch rib and tie girder structures, a comprehensive investigation was conducted to find the most effective section combinations that would satisfy design constraints while optimizing strength and minimizing weight. From Table 2, a series of sectional dimensions were given as an initial source of data for optimization analyses to find ideal sections for tie girders and arch ribs. Utilizing finite element analysis, a total of 64 combinations of sections for the arch ribs and tie girders were evaluated. Key structural responses including deflections, natural frequencies, axial forces, and bending moments were subsequently extracted from the analysis. Strength factors were then calculated to assess the adequacy of each combination under applied loads.

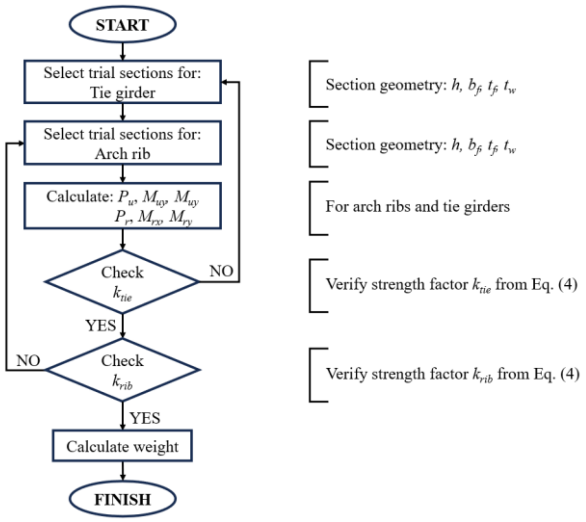

Fig. 8 Parametric optimization process for tie girders and arch ribs

Table 2
A source of sectional parameters for optimization

No.	h (mm)	b_f (mm)	t_w (mm)	t_f (mm)	A (mm^2)	I_x (mm^4)	I_y (mm^4)
1	150	125	8.5	14	4,537	17.5×10^6	4.56×10^6
2	200	150	9	16	6,312	44.3×10^6	9.01×10^6
3	250	125	10	19	6,870	71.4×10^6	6.20×10^6
4	300	150	10	18.5	8,180	125×10^6	10.4×10^6
5	350	150	9	15	7,380	151×10^6	8.45×10^6
6	400	150	10	18	9,040	237×10^6	10.1×10^6
7	450	175	11	20	11,510	387×10^6	17.2×10^6
8	600	190	13	25	16,650	966×10^6	28.7×10^6

The results, given in Fig. 9, present the distribution of strength factors corresponding to various section combinations, with the total weight of the arch ribs and tie girders plotted on the horizontal axis against the strength factors on the vertical axis. Particularly notable are the results highlighted by red dots for section numbers 6, 7, and 8, delineating combinations that not only provide sufficient strength factors but also comply with all design constraints, as shown in Fig. 9a. To identify a target efficient section combination, a search algorithm was applied to detect the most optimal configuration among 64 evaluated combinations. This optimal combination was found to consist of section number 6 for the arch ribs and section number 2 for the tie girders, achieving a minimum structural weight of 96.8 kN. The optimal dimensions and section properties for the arch ribs and tie girders were presented in Table 3 as a benchmark to select target sections for the detailed design.

Table 3
Optimal section properties for arch ribs and tie girders

Items	h (mm)	b_f (mm)	t_w (mm)	t_f (mm)	A (mm^2)	I_x (mm^4)	I_y (mm^4)
Tie girder	200	150	9	16	6,312	44.3×10^6	9.01×10^6
Arch rib	400	150	10	18	9,040	237×10^6	10.1×10^6

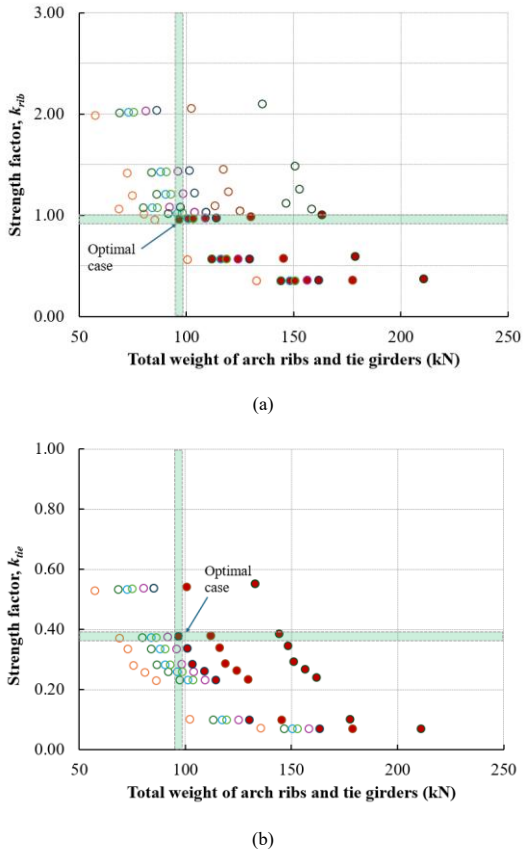

Fig. 9 Variation of strength factors in correlation with total weight: (a) for arch ribs; (b) for tie girders

2.2.4. Design of steel arch structures

The detailed design of the steel arch bridge progressed by finalizing sections that met the specified benchmarks for section properties as determined by optimization results. Table 4 provides a comprehensive overview of dimensions and section properties for all bridge components. Specifically, the section of the arch ribs was configured to have equal area and second moment of inertia compared to the optimal section, with an increased flange width aimed at enhancing out-of-plan bending stiffness. Furthermore, the design for tie girders exceeded the dimensions suggested by optimization results, driven by considerations of aesthetics and the need to mitigate deflection within the structure.

Table 4
Dimensions of structural components for detailed design

No.	h (mm)	b_f (mm)	t_w (mm)	t_f (mm)	A (mm^2)	I_x (mm^4)	I_y (mm^4)
Arch rib	390	200	10	14	9,220	237×10^6	18.7×10^6
Tie girder	300	200	10	14	8,320	131×10^6	18.7×10^6
Floor beam	200	100	5.5	8	2,612	17.6×10^6	1.33×10^6
Cross beam	250	160	10	10	5,500	56.2×10^6	6.84×10^6
Top brace	90	90	8	-	1,376	1.066×10^6	
Bottom brace	60	60	6	-	684	0.233×10^6	
Hanger rod	22	-	-	-	380	0.115×10^6	

Fig. 10 illustrates the overarching configuration of the steel arch structure, which incorporates approximately 17 tons of steel material. The selection of this material not only conferred a lightweight attribute upon the structure but also simplified logistical management throughout the construction phase. The I-shaped section of the arch rib was found to have a large slenderness which is sensitive to lateral buckling. Therefore, arch ribs, with large free length near bearings, were partially encased with UHPC to effectively improve the structure's stability and load-carrying capacity.

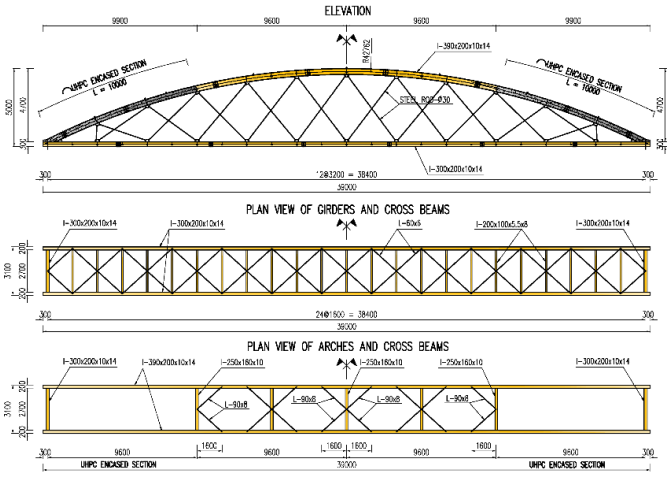

Fig. 10 General arrangement of steel structures: arches, girders, and cross beams

Fig. 11 shows the cross-sectional details of the steel arch ribs, illustrating both the steel section and the UHPC-encased section derived from the built-up I section design. The critical interaction between the UHPC and the steel section is achieved through the utilization of shear connectors positioned along the webs, ensuring an integrated structural behavior. The UHPC used in this design boasts a compressive strength of 100 MPa, providing exceptional durability and load-bearing capacity. This UHPC is made from a pre-mixed mortar and carefully cast in place to align precisely with the steel sections. This can improve the structural efficiency and strength of the arches.

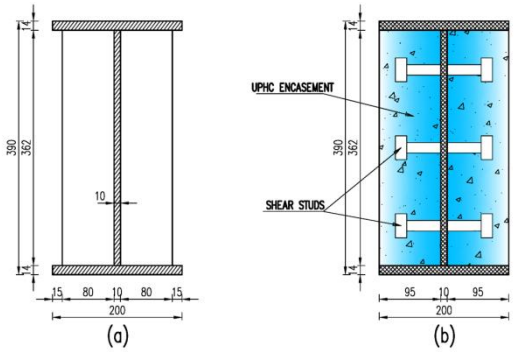

Fig. 11 Cross sections of arch ribs: (a) steel section; (b) UHPC encased section

3. Buckling analysis and verification

3.1. Finite element modeling

The steel arch structure, optimized in design, was analyzed using ABAQUS [28], to assess stability before construction. Models included steel sections and UHPC-encased sections to compare their instability behaviors. Steel arch members were modeled using 4-node quadrilateral stress/displacement shell elements (S4R) employing reduced integration and a large-strain formulation. The concrete parts were modeled using 8-node linear brick elements (C3D8R) with reduced integration and hourglass control. The hanger rods and bracing members of the vertical beams and arch were simplified using three-dimensional, 2-node truss elements (T3D2). For the UHPC encased parts, interaction between UHPC parts and arch ribs was controlled by using tie constraints along webs of arch ribs simulating shear connectors with the assumption that slip between the UHPC parts and steel web was negligible.

Fig. 12 illustrates the overall finite element model of the steel arch structure. The initial imperfection was considered as out-of-plan deformation δ_0 = 20 mm (0.05% of total span length) in the z-axis direction at the middle of the arch ribs. Boundary conditions were modeled according to the actual design with

four bearing positions. The entire arch system was supported by one fixed bearing, two unidirectional movable bearings, and one bidirectional movable bearing to ensure a simple support condition. Concentrated loads applied in finite element analysis were imposed in the middle of the span. To facilitate nonlinear analysis, a displacement-based method was utilized instead of force application. The imposed displacement values were gradually increased until structural failure occurs. Reaction forces measured at the displacement-controlled locations represented the corresponding forces acting on the structure. Fig. 13 illustrates parts of the finite element models of the arch members simulating the steel section, UHPC encasement, and tie constraints to generate composite interactions between steel web and concrete parts.

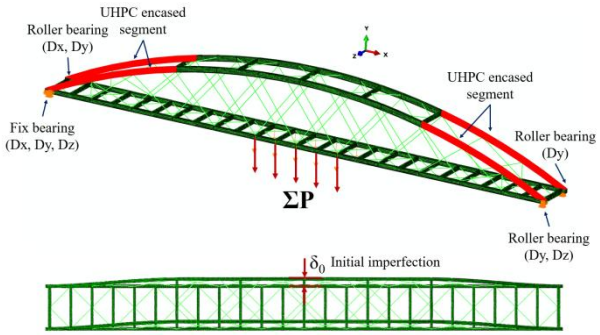

Fig. 12 General model of the steel arch with boundaries, loads, and imperfection

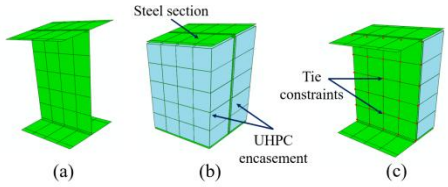

Fig. 13 Finite element models for steel arch members:
(a) steel section; (b) UHPC encased section; (c) tie constraints

Nonlinear analyses were conducted to investigate the steel arch's behavior considering nonlinear material modeling and applying large strain theory. The structural components, including the steel arch members and longitudinal beams, were constructed from SM490 steel plates, characterized by a yield strength of f_y = 390 MPa and a tensile strength of f_u = 560 MPa. The cross beams featured an I-shaped section and, along with the bracing members which are made of equal angle sections for both the arches and beam system, were fabricated from SS400 steel. This material was chosen for its yield strength of f_y = 290 MPa and ultimate strength of f_u = 460 MPa. Additionally, the hanger components were crafted from C45 steel bars, 22 mm in diameter, boasting a yield strength of f_y = 360 MPa and an ultimate strength of f_u = 610 MPa. The Young's modulus for all the steel materials used in the project was estimated to be 210,000 MPa, with a Poisson's ratio of 0.3. To ensure accuracy and reliability, stress-strain relationships for the verification models were derived from actual stress-strain curves obtained through material testing, whenever such data were available. Fig. 14 presents the stress-strain characteristic curves for the steel materials, utilizing a model that divides the curve into three linear segments. These curves, essential for the finite element analysis, were obtained from detailed studies on the steel materials' behavior. Initially, the material exhibits elastic behavior up to the yield strength and corresponding yield strain. Beyond this point, the material enters a yield plateau, maintaining the yield strength until the strain escalates to ten times the initial yield strain. Subsequently, the curve progresses to the tensile strength at an equivalent strain of 0.1. The Von-Mises yield criterion and isotropic hardening rule were used to model steel's behavior under different loads, providing a clear framework to predict its response to stress.

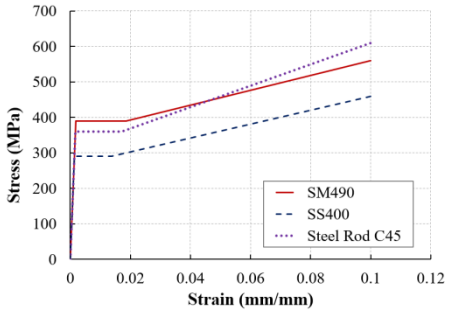

Fig. 14 Stress-strain relationship of steel materials for FEM analysis

In this study, UHPC was applied for composite interaction as encasement to improve the performance of steel arch members under compressive stresses. CEB-FIP Model Code [29] has proposed material models to simulate the behavior of the UHPC. The relation between stress σc and strain εc for short-term uniaxial compression is approximated by the following equation:

$$\frac{\sigma_c}{f_{cm}} = -\left(\frac{k\eta - \eta^2}{1+(k-2)\eta}\right) \quad \text{for} \quad |\varepsilon_c| < |\varepsilon_{c,\lim}| \tag{10}$$

where, $\eta = \varepsilon_c/\varepsilon_{c1}$ and $k = E_{ci}/E_{c1}$; f_{cm} is the actual compressive strength of concrete at an age of 28 days, $f_{cm} = f_{ck} + 8$ (MPa); f_{ck} is a specific characteristic compressive strength (MPa); ε_{c1} is the strain at maximum compressive stress; E_{c1} is the secant modulus from the origin to the peak compressive stress.

Crack opening was assumed to be small and was not considered in the analysis. For the uncracked normal weight concrete subjected to tension, a bilinear stress-strain relation is given as follows:

$$\sigma_{ct} = E_{ci}\varepsilon_{ct} \quad \text{for} \quad \sigma_{ct} \le 0.9 f_{ctm} \tag{11a}$$

$$\sigma_{ct} = f_{ctm}\left(1 - 0.1\frac{0.00015 - \varepsilon_{ct}}{0.00015 - 0.9 f_{ctm}/E_{ci}}\right) \quad \text{for} \quad 0.9 f_{ctm} < \sigma_{ct} \le f_{ctm} \tag{11b}$$

Where, E_{ci} is the tangent modulus of elasticity (MPa); ε_{ct} is the tensile strain; σ_{ct} is the tensile stress (MPa); f_{ctm} is the tensile strength (MPa).

Table 5
Material parameters of UHPC grade C100 given by Model Code [29]

Concrete grade	f_{ck} (MPa)	f_{ctm} (MPa)	E_{ci} (GPa)	E_{c1} (GPa)	ε_{c1} (‰)	$\varepsilon_{c,lim}$ (‰)
C100	100	5.2	47.5	36	3.0	3.0

The compressive strength of UHPC which was considered for the optimal design and finite element analyses was 100 MPa. Table 5 shows material parameters of UHPC grade C100 given by the Model Code [26] to construct the stress-strain diagrams in compression and tension. It is assumed that the maximum stress, f_{cm} = 108 MPa, was obtained at the proportional limit strain $\varepsilon_{c,lim}$ = 0.003. The value of tensile strength was approximated as f_{ctm} = 5.2 MPa to construct the stress-strain relation for UPHC in tension. Fig. 15 presents the approximated stress-strain diagrams of the UHPC derived from Eqs. (10) and (11) for the compressive strength and the tension strength, respectively.

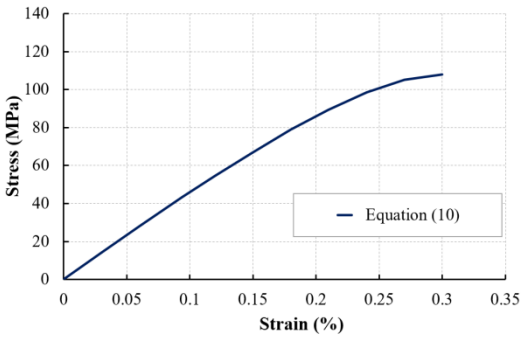

(a)

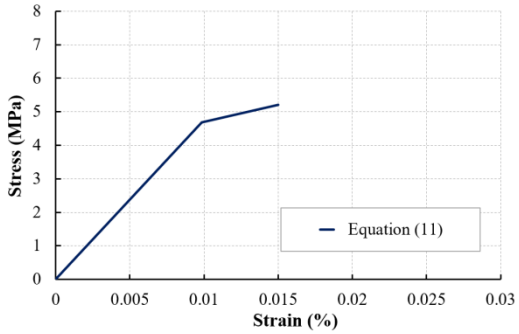

(b)

Fig. 15 Stress-strain diagrams of UHPC grade C100: (a) in compression; (b) in tension

3.2. Analysis results and verification

Fig. 16 illustrates the analytical outcomes derived from finite element analyses for two distinct scenarios involving arch ribs: one with a non-composite section and the other with a section encased in UHPC. The significance of points (a) and (c) lies in their representation of critical structural behaviors under peak loading conditions. Point (a) corresponds to the maximum load-carrying capacity of the non-composite section, recorded at 1,768.1 kN. This value indicates the limit at which the steel arch ribs begin to experience lateral buckling, leading to a rapid decrease in structural stability. Point (c), on the other hand, highlights the performance of the UHPC-encased section, with a maximum load-carrying capacity reaching 2,676.7 kN, an improvement of approximately 50% compared to the non-composite section. This significant increase is attributed to the UHPC encasement's ability to enhance the stiffness and reduce the susceptibility to lateral buckling, particularly in the critical regions near the bearings.

The comparison underscores the effectiveness of the UHPC encasement in mitigating lateral deformation and improving the overall structural resilience of the arch ribs. The inclusion of UHPC not only increases load-bearing capacity but also delays the onset of instability, thereby extending the operational safety margin of the structure. These findings validate the proposed design methodology and its potential applicability to similar projects requiring enhanced performance under constrained resources. By clearly indicating the importance of these points, Fig. 16 provides a visual representation of the substantial benefits achieved through UHPC integration in the design of steel arch bridges.

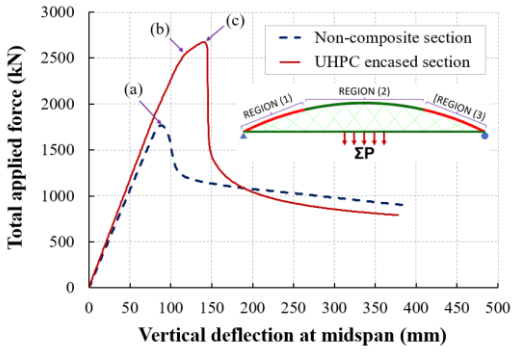

Fig. 16 Comparison of load-carrying capacity between steel section and UHPC encased section

In the study of a non-composite section under peak load conditions, Fig. 17 illustrates the progression of deformation in the steel arch alongside the corresponding loading states. Initially, it was observed that lateral buckling began to manifest subtly within the arch ribs. Specifically, the onset of yielding stress was identified at the edge regions of the top flange in designated areas (1) and (3), as depicted in Fig. 17a. This early sign of stress concentration was a precursor to more significant structural changes.

As the loading continued, these initial instances of lateral buckling evolved into pronounced out-of-plane deformations. These deformations were most notable in the middle sections of regions (1) and (3), where they expanded rapidly, as shown in Fig. 17b. This escalation in deformation led to a marked decrease in the structural integrity of the steel arch, culminating in an approximate 30% reduction in its load-carrying capacity.

The culmination of these structural changes led to the eventual failure of the steel arch. The complete breakdown was attributed to the lateral deformations within the steel arch members, specifically in the regions with large effective lengths - regions (1) and (3). These sections were identified as particularly susceptible to lateral buckling due to their structural characteristics. The sequence of deformation and failure, captured in Fig. 17c, underscores the critical impact of lateral buckling on the stability and performance of steel arch structures under significant load conditions.

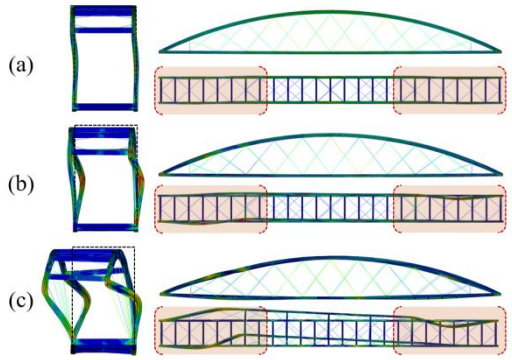

Fig. 17 Deformation and buckling behaviors of the steel arch: (a) at peak load; (b) after 30% drop; (c) at failure

In the case of the UHPC encased sections, the more vulnerable areas of the arch ribs were identified in region (2), where lateral buckling was a potential risk, particularly in unbraced sections of the arch. Observations from Fig. 18 indicate that the overall stiffness of the structure experienced a minor reduction starting from point (b), which corresponded to a total applied load of 2,535 kN. At this juncture, minor out-of-plane deformations began to manifest in the mid-sections of the arch ribs, accompanied by yielding of the top flanges because of maximum axial compression combined with bending, as illustrated in Fig. 18a.

As the stress continued to accumulate, it progressed toward the center of the web, peaking at point (c). This transition marks a critical phase where yielding stresses developed significantly between points (b) and (c), without the arch ribs undergoing instability, as depicted in Fig. 18b. Upon reaching peak load, out-of-plane deformations increased, especially in unbraced arch rib areas, reducing load capacity by 47% due to yielding and buckling effects (see Fig. 18c).

The most pronounced lateral deformations were observed in region (2), culminating in structural failure due to buckling in the sections comprised solely of steel, as evidenced in Fig. 18d. The analysis showed that encasing arch ribs in UHPC greatly improved stability and load-bearing capacity in regions (1) and (3), proving its effectiveness in strengthening these critical areas.

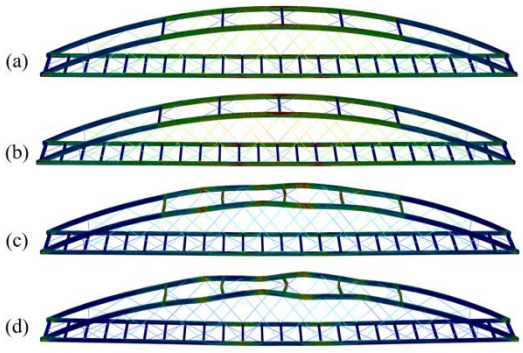

Fig. 18 Deformation of the steel arch with UHPC encased section: (a) at first yield; (b) at peak load; (c) after 47% drop of strength; (d) at failure

Figs. 19 and 20 illustrate the stress development and distribution within the steel arch under different scenarios: non-composite sections and UHPC-encased sections. These figures provide critical insights into how the integration of UHPC improves structural performance and mitigates vulnerabilities. To assess the impact of buckling in arch ribs, a critical location where buckling occurred was chosen for a comparative analysis of stress development between non-composite and UHPC encased sections. The analysis recorded stresses at seven points within these sections, correlating them with out-of-plane deflection.

In Fig. 19a, the stress distribution for the non-composite section shows significant disparities between the left and right sides of the arch ribs. This uneven stress distribution leads to pronounced in-plane and out-of-plane deformations, ultimately resulting in lateral buckling at peak load. Key stress concentrations are observed at points corresponding to the edges of the top flange, where instability initiates. The progression of stress and deformation underscores the limitations of the non-composite design in maintaining structural stability under high loads. Using the Von-Mises stress criterion, the stress in the non-composite section showed significant differences between the arch's sides as it approached 70 MPa, causing out-of-plane deformation and signs of instability. This instability was more pronounced with stresses reaching 90 MPa and 150 MPa at specific points, exacerbating the arch's in-plane and out-of-plane bending. At peak load, out-of-plane displacement reached 55 mm, and yielding started at around 150 mm, showing that arch instability was the main failure cause.

Fig. 19b shows the stress in the UHPC-encased section. UHPC reduces stress levels and distributes them more evenly, lowering bending effects and delaying buckling. At peak load, encased sections deflect about 20 mm, compared to 55 mm in the non-composite design, proving UHPC's effectiveness in improving structural strength. The results clearly demonstrate the effectiveness of UHPC encasement in reducing the stress experienced by the steel section. It was observed that the variation in stress levels between points 1 and 3, as opposed to points 2 and 4, attributable to transverse bending, was minimal. The peak load condition resulted in out-of-plane deformation of approximately 20 mm. Notably, the regions of the arch ribs reinforced with UHPC encasement showed no signs of instability, allowing the structure to reach its maximum load-bearing potential. Figure 20 shows the stress distribution at peak load for both scenarios. The non-composite section has high stress concentrations beyond the yield limit, causing rapid failure. In contrast, the UHPC-encased section keeps stress within safe limits, improving load capacity and stability. This highlights the benefits of UHPC encasement in enhancing the safety and durability of steel arches.

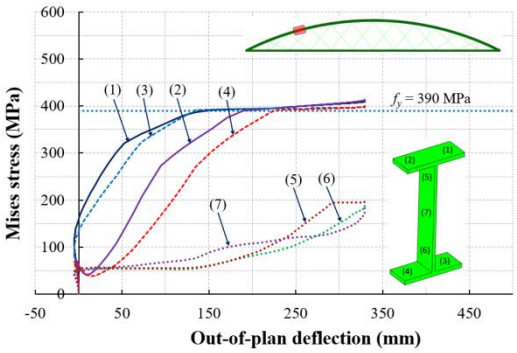

(a)

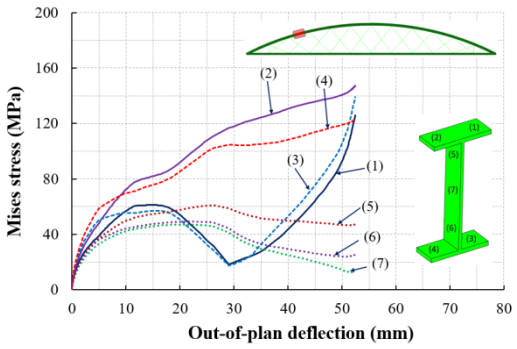

(b)

Fig. 19 Stress development: (a) Non-composite section with deformation; (b) UHPC-encased section with improved uniformity and reduced deformation

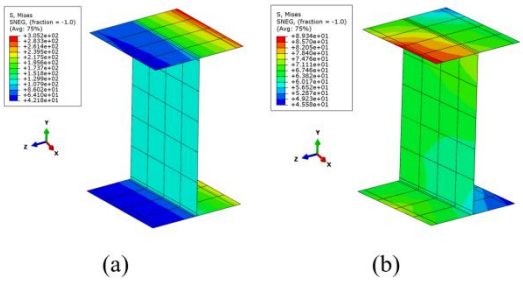

Fig. 20 Stress distribution at the peak load: (a) Non-composite section with high stress; (b) UHPC-encased section with improved stress

4. Application to a pilot construction project

4.1. Strength test for UHPC

The encasement process for the UHPC involved the use of a pre-mixed mortar that met the specified compressive strength requirements. This specific UHPC mix was developed through a prior study by Vinh et al. [30] and was selected for its robust characteristics for this pilot project. To ensure the material's strength met necessary standards, axial compression tests and tension tests were carried out before the UHPC was manufactured and transported to the site. The stress-strain relationships observed in these tests, as illustrated in Fig. 21, were then compared to theoretical predictions provided by the Model Code. The UHPC demonstrated a remarkable 28-day compressive strength of 118 MPa and a tensile strength of 6.8 MPa. The experimental results showed that the pre-mixed UHPC exceeded design standards and was approved for construction. A manually controlled intensive mixer ensured consistent quality and integrity during the mixing process.

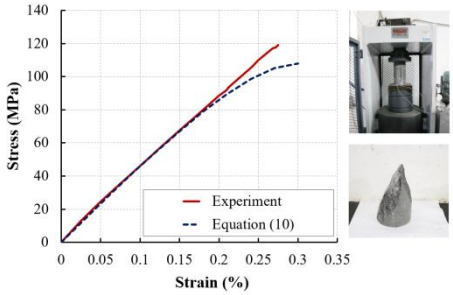

(a)

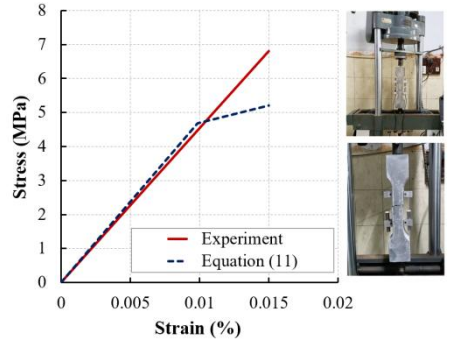

(b)

Fig. 21 Strength tests for pre-mixed UHPC: (a) compression test; (b) tension test

4.2. Fabrication of steel structures

Fig. 22 shows the steel structure manufacturing process in a factory. As this was the first use of the design, the process was carefully monitored, especially the welding. Non-destructive tests like ultrasonic testing (UT) and magnetic particle testing (MT) ensured the welds' quality. Furthermore, a trial assembly of the steel arch structure was carried out at the factory. This step was crucial for verifying the overall geometric accuracy and ensuring the compatibility of the various components that make up the steel arch. Considering the adoption of the incremental launching method for the structure's installation, a launching

nose equipped with a truss system was integrated with the steel arch during assembly. This procedure allowed for the testing of the structural launching process right at the factory, aiming to confirm both the feasibility of construction and the safety of the methodology.

Fig. 22 Fabrication and trial assembly of the steel structures at the factory

4.3. Construction implementation

Fig. 23 provides a visual guide to the steel arched bridge's erection sequence. Faced with several site-specific constraints, the construction team opted to assemble the steel structure entirely from one bank of the spring. This method effectively utilized the incremental launching technique, which was essential under the given conditions. A lightweight truss-equipped launching nose played a key role, while counterweights at the rear-maintained balance during construction. Pre-mixed UHPC mortar, produced in a factory, was intensively mixed to ensure quality and consistency before being delivered to the site. After assembling the steel framework, the UHPC encasement was carefully applied by hand, highlighting the precision and craftsmanship needed for this stage. Figure 23 shows the UHPC encasement in excellent condition at the end of construction, reflecting high-quality materials and workmanship. Load tests with actual service loads followed, ensuring the bridge's safety and functionality. These tests confirmed the structure's readiness for operation, marking a smooth transition from construction to service.

Fig. 23 Construction sequence of the pedestrian steel arched bridge

5. Conclusions

This study has presented an optimized design and construction scheme for steel arch pedestrian bridges enhanced with UHPC encasement, specifically developed to meet the demands of a resource-limited project in a remote area. By integrating UHPC with steel arches, the proposed method effectively mitigates lateral buckling and improves the load-carrying capacity and stability of the structure. Unlike prior studies, which often focus on large-scale or generic applications, this research uniquely addresses the practical challenges of constrained budgets and timelines, providing a tailored solution for underprivileged communities.

The successful implementation of the proposed design in an actual construction project highlights its practicality and impact. The bridge serves as a testament to the feasibility of advanced composite materials in addressing real-world challenges, offering a sustainable and cost-effective alternative to traditional construction methods. Furthermore, the findings provide a foundation for preliminary design guidelines, enabling practitioners to apply similar techniques in analogous projects. These contributions pave the way for future research aimed at refining the methodology and expanding its applicability to a broader range of infrastructure needs.

Looking forward, we acknowledge the need for further experimental validation and expanded case studies to enhance the robustness of the proposed approach. The research offers a foundational reference for engineers and designers seeking to explore innovative solutions in bridge construction, highlighting the potential for cost-effective, stable, and durable pedestrian bridge designs.

Acknowledgments

The authors gratefully acknowledge the support provided by Nam Phuong Foundation in collaboration with 3E Steel Technology and Engineering Company. Their financial and technical assistance has been invaluable to the completion of this work for the local people.

References

[1] Papangelis J.P., Trahair N.S., “Buckling of monosymmetric arches under point loads”, Engineering Structures, 10(4), 257-264, 1988.
[2] Pi Y.L., Trahair N.S., “Inelastic lateral buckling strength and design of steel arches”, Engineering Structures, 22(8), 993-1005, 2000.
[3] Pi Y.L., Trahair N.S., “Non-linear buckling and postbuckling of elastic arches”, Engineering Structures, 20(7), 571-579, 1998.
[4] Hu C.F., Li Z., Hu Q.S., “On non-linear behavior and buckling of arch-beam structures”, Engineering Structures, 239, 112-214, 2021.
[5] Han Q., Cheng Y., Lu Y., Li T., Lu P., “Nonlinear buckling analysis of shallow arches with elastic horizontal supports”, Thin-Walled Structures, 109, 88-102, 2016.
[6] Pi Y.L., Trahair N.S., “Non-linear buckling and postbuckling of elastic arches”, Engineering Structure, 20(7), 571-579, 1998.
[7] Pi Y.L., Bradford M.A., “Inelastic buckling and strengths of steel I-section arches with central torsional restraints”, Thin-Walled Structures, 41(7), 663-689, 2003.
[8] Dou C., Jiang Z.Q., Pi Y.L., Gao W., “Elastic buckling of steel arches with discrete lateral braces”, Engineering Structures, 156, 12-20, 2018.
[9] Dou C., Pi Y.L., “Flexural-torsional buckling resistance design of circular arches with elastic end restraints”, Journal of Structural Engineering, 142(2), 04015104, 2016.
[10] Nazmy A.S., “Stability and load-carrying capacity of three-dimensional long-span steel arch bridges”, Computers & Structures, 65(6), 857-868, 1997.
[11] Park J., Chun Y.H., Lee J., “Optimal design of an arch bridge with high performance steel for bridges using genetic algorithm”, International Journal of Steel Structures, 16, 559-572, 2016.
[12] Feng Y., Wang C., Briseghella B., Fenu L., Zordan T., “Structural optimization of a steel arch bridge with genetic algorithm”, Structural Engineering International, 31(3), 347-356, 2021.
[13] Latif M.A., Saka M.P., “Optimum design of tied-arch bridges under code requirements using enhanced artificial bee colony algorithm”, Advances in Engineering Software, 135, 102685, 2019.
[14] Pan W.H., Zhao C.H., Wang C.M., Luo Y.Z., “Optimal bracing system design for funicular twin arches against out-of-plane buckling”, Engineering Structures, 301, 117250, 2024.
[15] Zhang J.M., Wang C.M., Pan W.H., “Methodology for determining optimal design of funicular arches under point loads and selfweight against in-plane buckling”, Engineering Structures, 300, 117255, 2024.
[16] Bradford M.A., Pi Y.L., Qu W., “Time-dependent in-plane behaviour and buckling of concrete-filled steel tubular arches”, Engineering Structures, 33(5), 1781-1795, 2011.
[17] Jiang W., Lu D.G., “Reliability analysis for stability bearing capacity of CFST arches”, Proceedings of the 7th International Conference on Bridge Maintenance, Safety and Management, Shanghai, China, 2014.
[18] Huang F., Cui Y., Dong R., Wei J., Chen B., “Evaluation on ultimate load-carrying capacity of concrete-filled steel tubular arch structure with preload”, Advances in Structural Engineering, 22(13), 2755-2770, 2019.
[19] Sun J., Geng Y., Zhang H., Yin H., Wang Y., “Experimental and numerical study on slender concrete-filled steel tubular arches subjected to tilting loads”, Thin-Walled Structures, 179, 109701, 2022.
[20] Zhang Y., Liu A., Huang Y., Yang J., Fu J., Yu Y., Zeng X., “Experimental investigation of in-plane ultimate bearing capacity of parabolic high strength concrete-filled-steel-tubular arch”, Thin-Walled Structures, 183, 110348, 2023.
[21] Han X., Wei C., Hu Q., Liu C., Wang Y., “In-plane nonlinear buckling analysis and design method of concrete-filled steel tubular catenary arches”, Journal of Constructional Steel Research, 214, 108485, 2024.
[22] Zhou M., Lu W., Song J., Lee G.C., “Application of ultra-high-performance concrete in bridge engineering”, Construction and Building Materials, 186, 1256-1267, 2018.
[23] Chang C.M., Hossain A., “Life-Cycle Cost Analysis of Ultra High-Performance Concrete (UHPC) in Retrofitting Techniques for ABC projects”, Accelerated Bridge Construction University Transportation Center, 3-5, 2022.
[24] Dong Y., “Performance assessment and design of ultra-high performance concrete (UHPC) structures incorporating life-cycle cost and environmental impacts”, Construction and Building Material, 167, 414-425, 2018.
[25] Stengel T., Schießl P., “Life cycle assessment (LCA) of ultra high performance concrete (UHPC) structures”, Eco-efficient Construction and Building Materials, 528-564. Woodhead Publishing, 2014.
[26] AASHTO. LRFD Guide Specifications for the Design of Pedestrian Bridges. American Association of State Highway and Transportation Officials, Washington DC, 2009.
[27] AASHTO. AASHTO LRFD bridge design specifications. American Association of State Highway and Transportation Officials, Washington DC, 2012.
[28] ABAQUS. ABAQUS standard user’s manual version 6.5. Hibbit, Karsson and Sorensen Inc., 2005.
[29] Taerwe L., Matthys S., Fib model code for concrete structures 2010, Ernst & Sohn, Wiley, 2013.

[30] Chu V.T.H., Bui V.D., Nguyen T.V., "Effect of aggregate grading and steel fiber on the properties of ultra-high performance fiber reinforced concrete". Proceedings of the International Conference on Sustainable Civil Engineering and Architecture, Singapore, 2023.